The Astrophysical Journal, 826:31 (8pp), 2016 July 20 doi:10.3847/0004-637X/826/1/31

THE GIGAELECTRONVOLT COUNTERPART OF VER J2019+407 IN THE NORTHERN SHELL OF THE SUPERNOVA REMNANT G78.2+2.1 (γ Cygni)

N. Fraija[1] and M. Araya[2]
[1] Instituto de Astronomía, Universidad Nacional Autónoma de México, Apdo. Postal 70-264, Cd. Universitaria, DF 04510, México; nifraija@astro.unam.mx
[2] Escuela de Física & Centro de Investigaciones Espaciales (CINESPA), Universidad de Costa Rica, San José 2060, Costa Rica; miguel.araya@ucr.ac.cr
Received 2016 February 2; revised 2016 May 2; accepted 2016 May 2; published 2016 July 18

ABSTRACT

Analysis of gamma-ray emission from the supernova remnant G78.2+2.1 (γ Cygni) with 7.2 years of cumulative data from the Fermi Large Area Telescope shows a distinct hard, bright, and extended component to the north of the shell coincident with the known teraelectronvolt source VER J2019+407. In the gigaelectronvolt to teraelectronvolt (GeV–TeV) energy range, its spectrum is best described by a broken power law with indices 1.8 below a break energy of 71 GeV and 2.5 above the break. A broadband spectral energy distribution is assembled, and different scenarios for the origin of the gamma rays are explored. Both hadronic and leptonic mechanisms are able to account for the GeV–TeV observations. In the leptonic framework, a superposition of inverse Compton and nonthermal bremsstrahlung emissions is needed, whereas the hadronic scenario requires a cosmic-ray population described by a broken power-law distribution with a relatively hard spectral index of ∼1.8 below a break particle energy of 0.45 TeV. In addition, the neutrino flux expected from cosmic-ray interactions is calculated.

Key words: acceleration of particles – ISM: individual objects (G78.2+2.1) – ISM: supernova remnants – radiation mechanisms: nonthermal

1. INTRODUCTION

Supernova remnants (SNRs) are believed to be the sites where cosmic rays (CRs) in our galaxy are accelerated up to approximately petaelectronvolt energies. Studying the gigaelectronvolt to teraelectronvolt (GeV–TeV) γ-ray emission from SNRs is important to shed light on the puzzle of the origin of these high-energy (HE) particles that populate the Galaxy. The mechanism of diffusive shock acceleration (e.g., Bell 1978; Blandford & Eichler 1987) is thought to play an important role in transferring some of the kinetic energy from an SNR's expansion to particles. The shocks of SNRs are known to accelerate electrons up to very high energies (VHEs). In the leptonic framework, electron synchrotron radiation is emitted from radio wavelengths to X-rays (e.g., Ammosov et al. 1994; Gotthelf et al. 2001; Berezhko et al. 2002; Hwang et al. 2002; Rho et al. 2002), and inverse Compton (IC) scattering and bremsstrahlung emissions are emitted in gigaelectronvolt γ-rays. In the hadronic picture, CR protons (or nuclei) can produce GeV–TeV γ-rays through the decay of neutral pions produced in photon–hadron interactions as well as hadronic collisions with ambient material. Therefore, spectral and morphological studies of γ-ray data can be used in principle to disentangle the nature of the particles involved. Although, during the last several years, many SNRs have been detected in γ-rays (e.g., Abdo et al. 2009, 2010b, 2010c, 2010d, 2010e, 2010f; Ellison et al. 2010; Ackermann et al. 2011; Yuan et al. 2011; Tanaka et al. 2011; Ajello et al. 2012; Araya 2013, 2014, 2015), it is not clear which emission mechanism dominates in most cases. In some SNRs the γ-ray emission is coincident with high-density ambient clouds, and its spectral shape can be described by the hadronic scenario, although details on the predicted spectral shape are still debated, and the ambient properties are usually poorly known.

Some related teraelectronvolt sources are pulsar wind nebulae, the relativistic magnetized winds (mostly $e^{\pm}$ pairs, associated with a pulsar) that create termination shocks where particle acceleration occurs. Their spectral energy distributions (SEDs) are dominated by synchrotron and IC scattering from HE leptons, although hadronic processes may also contribute (Cheng et al. 1990; Amato et al. 2003). On the other hand, however, the nature of many of the VHE sources remains unknown. Such is the case of the source VER J2019+407 (Aliu et al. 2013).[3] At teraelectronvolt energies this source has an extent of $0.^{\circ}23 \pm 0.^{\circ}03_{\rm stat}{}^{+0.^{\circ}04}_{-0.^{\circ}02{\rm sys}}$, and its γ-ray spectrum is described by a simple power law (Aliu et al. 2013).

VER J2019+407 is found within the radio shell of the SNR G78.2+2.1 in spatial coincidence with nonthermal radio emission (Ladouceur & Pineault 2008). Located at (1.5-1.8) kpc and seen at ∼2.°5 from the star-forming region Cygnus X (e.g., Wendker et al. 1991), it is ∼1° in diameter (Higgs 1977; Higgs et al. 1977; Landecker et al. 1980; Lozinskaya et al. 2000). The SNR shows a distinctive shell in radio wavelengths and X-rays with brighter northern and southern regions (Downes & Rinehart 1966; Higgs 1977; Brazier et al. 1996; Zhang et al. 1997; Kothes et al. 2006; Leahy et al. 2013). Most of the radio flux comes from the southeastern part of the remnant. Higher radio spectral indices (steeper spectra) are seen near the center of the remnant (although they could be associated with the shell) and around the shock of the SNR (Zhang et al. 1997). Several studies have found that the average radio spectral index is around 0.5 (e.g., Pipenbrink & Wendker 1988; Kothes et al. 2006), but a detailed analysis of the ambient thermal emission and the synchrotron radiation of the remnant with high-sensitivity data from the Canadian Galactic Plane Survey (CGPS; Taylor et al. 2003) has yielded a significantly larger average spectral index of 0.75 ± 0.3 with spatial variations from 0.40 to 0.80 (Ladouceur & Pineault 2008). There is evidence that the nonthermal radio emission at the location of the teraelectronvolt source VER J2019+407 has a spectrum that is harder than average, with a spectral index close to 0.40 (Zhang et al. 1997).

[3] See also the catalog of TeV sources at http://tevcat.uchicago.edu.

Neutral hydrogen emission has been observed and associated with the SNR, including postshock H I to the south and northeast of the SNR (Landecker et al. 1980; Braun & Strom 1986), as well as a shell around the SNR with an estimated density of 2.5 cm^{-3} that might have been produced by the stellar wind of the SNR progenitor (Gosachinskij 2001). No evidence has been found of interactions with molecular gas in a CO survey (Higgs et al. 1983). However, Fukui & Tatematsu (1988) observed a CO cloud that was associated with the southeastern section of the SNR, and Pipenbrink & Wendker (1988) found H_2CO absorption, indicating the presence of dense material in this zone. A large thermal radio feature and several small H II regions are imaged near and overlapping parts of the SNR, among them the H II region known as the γ Cygni nebula coincident in position with the brightest nonthermal emission to the southeast of the SNR (Higgs 1977; Wendker et al. 1991). Requiring a distance of 1.7 kpc, X-ray and Hα observations have yielded a shock velocity of (1–1.5) $\times$ 10^3 km s^{-1}, an unperturbed number density of (0.14–0.3) cm^{-3}, a temperature of (1.6–3.2) $\times$ 10^7 K for the X-ray-emitting gas in the bright shell, and a remnant age of 4000–6000 years, assuming an explosion kinetic energy of 10^{51} erg (Lozinskaya et al. 2000). Analyzing optical data of bright regions, Mavromatakis (2003) found a shock speed of 750 km s^{-1}, an age of 7000 years, and unperturbed interstellar medium (ISM) densities of 0.3 cm^{-3} containing compressed clouds with densities of ~700 cm^{-3} (corresponding to preshock densities of ~20 cm^{-3}). Based on ASCA X-ray observations, Uchiyama et al. (2002) derived a shock velocity of 800 km s^{-1} and an adiabatic age of 6600 years, assuming a distance of 1.5 kpc. These authors also discovered two clumps (labeled C1 and C2) of hard X-ray emission to the north of the SNR. These were attributed to nonthermal bremsstrahlung radiation from electrons in shocked dense cloudlets with gas density between 10 and 100 cm^{-3}. An analysis of *INTEGRAL*-ISGRI (Bykov et al. 2004) revealed hard X-ray clumps of about 10 arcmin in size in the northwest (the most prominent one), the southeast, and the northeast regions of the SNR. These are compatible with both the ASCA fluxes derived by Uchiyama et al. (2002) and the spatially unresolved *RXTE* Proportional Counter Array (PCA) data (Bykov et al. 2004). The observed spatial morphology and spectra are consistent with the emission generated by nonthermal electrons accelerated at the shock of a supernova interacting with an interstellar cloud. Using a *Chandra* observation of the region (Leahy et al. 2013), it was found later that C1 is extended and likely associated with an extragalactic object, whereas C2 has an absorption column density that is in agreement with the location of the SNR and a nonthermal, power-law spectrum with index of ~1.0 (Leahy et al. 2013). C2 is located within the extent of VER J2019+407.

Gamma-ray emission in the region of G78.2+2.1 was detected by the EGRET instrument on board the Compton Gamma Ray Observatory (Thompson et al. 1995). The Large Area Telescope (LAT) on board the Fermi Gamma-ray Space Telescope satellite has found extended emission from this remnant (Lande et al. 2012) and also discovered a bright γ-ray pulsar, PSR J2021+4026, near the center of the remnant (Abdo et al. 2010a, 2010g). G78.2+2.1 is also near the Cygnus Cocoon, an extended region of freshly accelerated CRs seen by the Fermi satellite above 1 GeV (Ackermann et al. 2011) that also shows teraelectronvolt emission (Abdo et al. 2007; Bartoli et al. 2014). The SNR could be a source of at least some of the HE particles in the cocoon (Ackermann et al. 2011; Abdo et al. 2007).

Although the γ-ray emissions from both the SNR and the pulsar PSR J2021+4026 are difficult to disentangle at a few gigaelectronvolts, the flux from the SNR becomes dominant above ~10 GeV as the spectrum of PSR J2021+4026 follows a power law with an exponential cutoff with a cutoff energy of ~2.4 GeV. In the latest LAT catalog, the morphology of the emission from the entire shell of the SNR, also called 3FGL J2021.0+4031e (Acero et al. 2015), has been described with a uniform disk of radius $0\overset{\circ}{.}63$ centered at the position (J2000) $\alpha = 305\overset{\circ}{.}27$, $\delta = 40\overset{\circ}{.}52$. In this paper, we report the discovery of an extended region of enhanced gigaelectronvolt emission that is spatially coincident with the teraelectronvolt source VER J2019+407 using LAT data. This paper is arranged as follows. We describe the data analysis in Section 2 and the results in Section 3. In Section 4 we present the calculations of the models for the nonthermal emission and the expected neutrino flux. Our discussion is given in Section 5 and the conclusions in Section 6. We hereafter use $k = \hbar = c = 1$ in natural units and adopt a source distance of 1.5 kpc.

2. FERMI LAT OBSERVATIONS

LAT data selected in the energy range 4–300 GeV and acquired from the beginning of the mission, 2008 August to 2015 November, are analyzed with the most recent software SCIENCETOOLS version v10r0p5[4] and reprocessed with "Pass 8" photon and spacecraft data (Atwood et al. 2013) and the instrument response functions P8R2_SOURCE_V6P.

Photons are selected within a square region of $20^\circ \times 20^\circ$ centered at the coordinates (J2000) $\alpha = 305\overset{\circ}{.}34$, $\delta = 40\overset{\circ}{.}43$ (the region of interest, hereafter ROI). As indicated above, the analysis is restricted to energies above 4 GeV in order to avoid the bright emission from the pulsar PSR J2021+4026. Standard cuts are applied in the analysis, including selecting zenith angles less than 90° to remove photons from the Earth limb and keeping the SOURCE class events. Time intervals are selected when the LAT instrument was in science operations mode, and the data quality was good. The data are binned in 20 logarithmically spaced bins in energy, and a spatial binning of $0\overset{\circ}{.}02$ per pixel is used.

The analysis of LAT data is performed by a method of maximum likelihood that estimates the probability of reproducing the spectral and morphological properties of sources with a given model (Mattox et al. 1996). The model initially contains the sources present in the latest LAT catalog (Acero et al. 2015) as well as the standard diffuse Galactic emission template and the isotropic emission that accounts for extragalactic background and misclassified CRs. In all the likelihood fits, the normalizations of these components are kept free, as are the normalizations of sources located less than six degrees from the center of the ROI, except for those sources that are detected below the 5σ level above 4 GeV, in which case their spectral parameters are kept fixed to the cataloged values. The effect of freeing the normalization of the PSR J2021+4026 spectrum inside the shell of G78.2+2.1 is evaluated.

[4] See http://fermi.gsfc.nasa.gov/ssc.

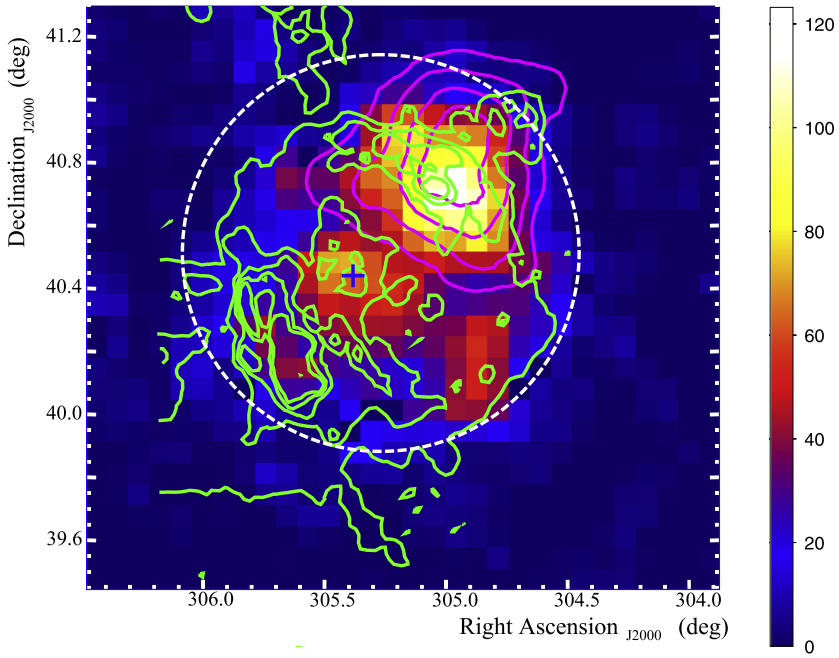

Figure 1. Significance map, in units of TS, of the G78.2+2.1 region for γ-rays above 15 GeV with a scale of ~0.067 deg/pixel. The CGPS 1420 MHz observation is represented by green contours at brightness temperatures of 22, 31.5, 41, 50.5, and 60 K. The VER J2019+407 smoothed photon excess contours (100, 150, 210, and 260 photons) are shown in magenta. The location of the γ-ray pulsar PSR J2021+4026 is marked with a blue cross, and the boundary of the 3FGL J2021.0+4031e disk is displayed by the white dashed circle.

3. RESULTS

From the LAT data analysis described above, we conclude that a uniform disk is not a good description of the γ-ray morphology of G78.2+2.1. If the source 3FGL J2021.0 +4031e is not included in the model, the resulting residuals show a morphology that is quite unlike that of a uniform disk, which was reported in the LAT catalog for this source. Even when we incorporate this source in the model, the resulting residuals show a clear excess in the northern region of the SNR. To study this emission further, a significance map is calculated above 15 GeV with the tool gttsmap for a square region of $2^\circ \times 2^\circ$ around the position of the SNR. The map, shown in Figure 1, is in units of test statistic (TS), which is defined as twice the logarithm of the ratio of maximum likelihood values obtained with a point source located at each pixel position and that obtained with no source. The associated significance at each position is then $\sim\sqrt{\mathrm{TS}}$ (Mattox et al. 1996). The TS map in Figure 1 shows the radio contours from a CGPS observation of G78.2+2.1 as well as the significance contours of the teraelectronvolt source VER J2019+407 (Aliu et al. 2013). The same region of enhanced emission seen in the residuals map is clearly visible in the TS map, which coincides with the location of VER J2019+407.

The excess found in the northern shell of the SNR is extended, as shown by residuals obtained after placing a point source at the position of maximum TS in the significance map. Because of the previous result and the location of the excess in coincidence with VER J2019+407, it is natural to associate the gigaelectronvolt with the teraelectronvolt source. We adopt the spatial morphology used to describe the teraelectronvolt emission from VER J2019+407 (Aliu et al. 2013) as a template for the emission detected by the LAT telescope, which is a symmetric two-dimensional Gaussian with an extension of $0.^\circ23$ and centroid coordinates of (J2000) $\alpha = 305.^\circ02$, $\delta = 40.^\circ76$.

The rest of the emission from the SNR around the position of VER J2019+407 has to be taken into account in the model to accurately describe the properties of the source. We then use a spatial template obtained from removing a $0.^\circ23$ radius circular region around VER J2019+407 from the disk of 3FGL J2021.0 +4031e to represent the southern part of γ Cygni and the rest of the SNR's shell. We fit the data above 4 GeV by adopting power-law spectra for both components with free parameters. The resulting TS values for VER J2019+407 and the southern region are 180 and 400, respectively. The power-law indices and fluxes are 1.91 ± 0.10 and $(7.61 \pm 0.84) \times 10^{-10}$ ph cm^{-2} s^{-1} for VER J2019+407, and 1.93 ± 0.06 and $(2.47 \pm 0.17) \times 10^{-9}$ ph cm^{-2} s^{-1} for the southern region. It is important to note that these parameters are derived for events in the 4–300 GeV band, while the TS map plotted in Figure 1 was obtained above 15 GeV in order to avoid contamination from the bright pulsar near the center of the SNR. Even above 10 GeV, the pulsar is detected at almost the 11σ level. The determination of the spectral parameters of the southern shell is affected by the pulsar emission. It is found that freeing the spectral normalization of the pulsar model in the fit results in a spectral index for the southern shell of 2.04 ± 0.06 without considerably affecting the results for VER J2019+407. The study of the effect of the pulsar emission in the region beyond the extension of VER J2019+407 is outside the scope of this paper, and thus we cannot conclude if the spectrum of VER J2019+407 is harder than that of the rest of the shell around several gigaelectronvolts. However, VER J2019+407 seems to show a harder LAT spectrum above ~10 GeV. In count maps of increasing energy, the emission of the source certainly dominates over the rest of the shell, which is also consistent with the nondetection of teraelectronvolt photons around this

region (Aliu et al. 2013), and, in the 10–300 GeV (15–300 GeV) range, the spectral indices for VER J2019 +407 and the rest of the shell are 2.07 ± 0.17 and 2.20 ± 0.10 (2.1 ± 0.2 and 2.35 ± 0.15), respectively.

The LAT spectrum of VER J2019+407 is not curved in the energy range analyzed here. Assuming either a log parabola or a power law with an exponential cutoff for the spectrum results in the same source significance as the one obtained with a simple power law.

In order to construct the LAT SED, we binned the data in 16 logarithmically spaced energy intervals from 4 to 300 GeV and also applied a likelihood fit in each interval. When the TS of the source falls below nine, a 95% confidence level upper limit on the flux is calculated in the corresponding interval. In each bin, the spectral normalization of the pulsar is set to free to compare results when it is kept frozen to the cataloged value. The effect of the pulsar on VER J2019+407 is only important in the first energy bin (4–5.5 GeV), where it results in a 10% variation of the flux from the source. This is considered as a systematic error in this bin.

A careful analysis of the LAT observation to decrease the effect of the contamination from photons from the bright nearby pulsar PSR J2021+4026, for example using "front" events with an improved point-spread function (PSF), which is beyond the scope of this work, is needed to study the emission of the SNR below a few gigaelectronvolts. We carried out a preliminary fit to the LAT data only, above 1 GeV, and found an indication that the photon spectrum becomes softer at lower energies. Using the same spatial template for VER J2019+407, the fit yields a power-law spectrum with index $2.22 \pm 0.08_{\rm stat}$.

3.1. Multiwavelength SED

We gathered data from the literature to assemble the multiwavelength SED. The radio fluxes are used for the integrated emission from the entire SNR (Higgs et al. 1977; Wendker et al. 1991; Zhang et al. 1997; Kothes et al. 2006; Gao et al. 2011) for reference. The 10.6 GHz flux from a $7' \times 9'$ region within VER J2019+407 is taken from a previous study (Higgs 1977) as the expected radio synchrotron flux from the northern shell of G78.2+2.1. The X-ray data are taken from *RXTE* PCA and ASCA observations of the entire SNR (Bykov et al. 2004), and the ASCA fluxes from the hard X-ray clumps are from Uchiyama et al. (2002). The *INTEGRAL*-ISGRI fluxes from another clump of hard emission to the northwest of the SNR (Bykov et al. 2004) are also shown.

4. EMISSION MODEL

The emission models and particle distributions used to account for the broadband SED of VER J2019+407 are summarized next. We use a simple one-zone model that includes standard radiation mechanisms from leptons and hadrons. In all the broadband models, the emitting region is taken as spherical with a radius of 0°.23, which at a distance of 1.5 kpc corresponds to a physical radius of 6 pc.

4.1. Synchrotron Radiation

In the relativistic case, the electron population is given by $N(E_{\rm e}) \propto E_{\rm e}^{-\alpha_{\rm e}}$ where $\alpha_{\rm e}$ is the spectral index and $E_{\rm e}$ the particle energy. We assume this distribution cuts off above a certain energy. The electrons in the emitting region permeated by a magnetic field B cool down in a timescale given by the standard cooling time $\tau_c = \frac{6\pi m_{\rm e}^2}{\sigma_T} B^{-2} E_{\rm e}^{-1}$, with $\sigma_T = 6.65 \times 10^{-25}\,{\rm cm}^2$ the Compton cross section and $m_{\rm e}$ the electron mass. Equating the synchrotron timescale with the age of the source $\tau_{\rm age}$ (Uchiyama et al. 2002; Fraija 2014a), we get that the cooling break energy is $E_{e,{\rm br}} = \frac{6\pi m_{\rm e}^2}{\sigma_T} B^{-2}\,\tau_{\rm age}^{-1}$, and then the cooling synchrotron break energy is

$$\epsilon_{\gamma,{\rm br}}^{\rm syn} = \frac{36\pi^2\, q_{\rm e}\, m_{\rm e}}{\sigma_T^2}\, B^{-3}\, \tau_{\rm age}^{-2}. \quad (1)$$

The synchrotron spectrum is computed by summing over the electron distribution. The photon energy radiated in the range ϵ_γ to $\epsilon_\gamma + d\epsilon_\gamma$ is given by electrons with energies between $E_{\rm e}$ and $E_{\rm e} + dE_{\rm e}$. Then the photon spectrum can be estimated through the emissivity $[\epsilon_\gamma F(\epsilon_\gamma) d\epsilon_\gamma]_{\gamma,{\rm syn}} = (-dE_{\rm e}/dt) N_{\rm e}(E_{\rm e}) dE_{\rm e}$, with $F(\epsilon_\gamma) = \left[\frac{dN(\epsilon_\gamma)}{d\epsilon_\gamma}\right]_{\gamma,{\rm syn}}$ the differential synchrotron photon flux.

4.2. Inverse Compton Scattering

Electrons accelerated at shock fronts can upscatter external photons up to higher energies. The synchrotron and IC scattering fluxes are given by (Aharonian et al. 1997)

$$[\epsilon_\gamma^2 F(\epsilon_\gamma)]_{\gamma,{\rm IC}} = \frac{U_{\rm syn}}{U_B} [\epsilon_\gamma^2 F(\epsilon_\gamma)]_{\gamma,{\rm syn}}, \quad (2)$$

with $F(\epsilon_\gamma) = \left[\frac{dN(\epsilon_\gamma)}{d\epsilon_\gamma}\right]_{\gamma,{\rm IC}}$ the differential Compton scattering photon flux, and $U_{\rm syn}$ and $U_B = \frac{B^2}{8\pi}$ are the energy density of the synchrotron radiation and magnetic field, respectively. Considering the energy density of the cosmic microwave background (CMB) radiation (Aharonian et al. 1997), the fluxes of synchrotron radiation at radio wavelengths and IC scattering in γ-rays are related by

$$[\epsilon_\gamma^2 N(\epsilon_\gamma)]_{\gamma,{\rm IC}} = \frac{U_{\rm CMB}}{U_B} [\epsilon_\gamma^2 N(\epsilon_\gamma)]_{\gamma,{\rm syn}}, \quad (3)$$

with $U_{\rm CMB} = 0.25\ {\rm eV\ cm^{-3}}$.

4.3. Nonthermal Bremsstrahlung

The Coulomb energy-loss rate of relativistic electrons, $dE/dt \propto 3\, n_{\rm e}\, \sigma_T\, m_{\rm e}\, v^{-1} \ln\Lambda/2$ (Rephaeli 1979), is proportional to the gas density $n_{\rm e}$ and independent of the electron energy, where v is the velocity of nonthermal electrons and Λ the Coulomb logarithm. Comparing the cooling time of electrons due to Coulomb interactions and the age of the object $\tau_{\rm age}$, we get that the Coulomb break kinetic energy is (Uchiyama et al. 2002)

$$K_{\rm Cou} = \frac{3}{2}\sigma_T\, m_{\rm e}\, n_{\rm e}\, v^{-1} \ln\Lambda\, \tau_{\rm age}. \quad (4)$$

The differential energy spectrum of the bremsstrahlung emission from accelerated electrons is given by (Blumenthal & Gould 1970)

$$[F(\epsilon_\gamma)]_{\gamma,{\rm Cou}} \simeq \int dE_{\rm e}\, N(E)\beta \times \left(n_{\rm p}\frac{d\sigma_{\rm eH}}{d\epsilon} + n_{\rm He}\frac{d\sigma_{\rm eHe}}{d\epsilon} + n_{\rm e}\frac{d\sigma_{\rm ee}}{d\epsilon}\right), \quad (5)$$

where $n_{\rm p}$, $n_{\rm He}$, and $n_{\rm e}$ are the hydrogen, helium, and electron number densities, respectively, $d\sigma/d\epsilon$ is the differential cross section for emitting a bremsstrahlung photon in the energy interval ϵ to $\epsilon + d\epsilon$, and $F(\epsilon_\gamma) = \left[\frac{dN(\epsilon_\gamma)}{d\epsilon_\gamma}\right]_{\gamma,\rm Cou}$ is the differential bremsstrahlung photon flux.

4.4. Proton–Proton Interactions

HE protons accelerated in shock fronts can interact with ambient protons, producing neutral and charged pions and mesons (Stecker 1973). For the accelerated CR distribution we adopt several possibilities, including a standard power law in momentum, p, $\frac{dN_{\rm p}}{dp} = K_{\rm p}\, p^{-\alpha_{\rm p}}$, a power law with an exponential cutoff, $\frac{dN_{\rm p}}{dp} = K_{\rm p}\, p^{-\alpha_{\rm p}} e^{-\frac{p}{p_c}}$, and a broken power-law distribution, given by

$$\frac{dN_{\rm p}}{dp} = K_{\rm p}\left[1 + \left(\frac{p}{p_{\rm br}}\right)^2\right]^{-\frac{\Delta\alpha_{\rm p}}{2}} \left(\frac{p}{p_0}\right)^{-\alpha_{\rm p}} \quad (6)$$

with $\Delta\alpha_{\rm p} = \beta_{\rm p} - \alpha_{\rm p}$. In these functions, $K_{\rm p}$ is a normalization constant, p_0 is a scale constant, p_c is the cutoff momentum, and p_{br} is the break momentum. We denote the corresponding cutoff and break energies in the γ-ray spectrum as $\epsilon^{\rm pp}_{\gamma,c}$ and $\epsilon^{\rm pp}_{\gamma,br}$. Evidence in favor of this kind of proton distribution is seen in systems where SNRs interact with ambient material (e.g., Abdo et al. 2009).

If the proton distribution is converted to the total particle energy ($E_{\rm p}$) space by $\frac{dN_{\rm p}}{dE_{\rm p}} = \frac{dN_{\rm p}}{dp}\frac{dp}{dE_{\rm p}} = \frac{E_{\rm p}}{p}\frac{dN_{\rm p}}{dp}$, the total energy content in protons can be calculated as

$$U = V\, W_{\rm p} = V \int_{E_{\rm p,min}}^{E_{\rm p,max}} E_{\rm p}\, \frac{dN_{\rm p}}{dE_{\rm p}} dE_{\rm p}, \quad (7)$$

where the particles are assumed to be uniformly distributed in a volume $V = \frac{4}{3}\pi R^3$ with radius R. The total hydrogen mass inside this volume is $M_{\rm H} = n_{\rm p}\, m_{\rm p}\, V$.

4.4.1. GeV–TeV γ-ray Spectrum

The γ-ray spectrum produced by hadronic collisions is given by (Kelner et al. 2006)

$$\left(\frac{dN_\gamma}{dE_\gamma}\right) = \frac{V}{4\pi d_z^2} n_{\rm p} \int_{E_\gamma}^{\infty} \sigma_{\rm pp}(E_{\rm p}) \frac{dN_{\rm p}}{dE_{\rm p}} F_\gamma^{\rm pp}(E_{\rm p}, x) \frac{dE_{\rm p}}{E_{\rm p}}, \quad (8)$$

where $d_z = 1.5$ kpc is the distance to VER J2019+407, $\sigma_{\rm pp}(E_{\rm p}) = 34.3 + 1.88\, S + 0.25\, S^2$ mb is the cross section for these interactions where $S = \log(E_{\rm p}/1\ {\rm TeV})$, and $F_\gamma^{\rm pp}(E_{\rm p}, x)$ is given in Kelner et al. (2006). It is noted that at high energies the gamma-ray spectrum maps the particle spectrum, which could in principle be used to discriminate between different spectral functions.

4.4.2. Neutrino Emission

Charged pions produced in hadronic collisions decay into electrons/positrons and neutrinos: $\pi^\pm \rightarrow \mu^\pm + \nu_\mu/\bar{\nu}_\mu \rightarrow e^\pm + \nu_\mu/\bar{\nu}_\mu + \bar{\nu}_\mu/\nu_\mu + \nu_e/\bar{\nu}_e$. The spectrum of muon neutrinos generated by these interactions is given by (Kelner et al. 2006)

$$\left(\frac{dN_\nu}{dE_\nu}\right) = \frac{V}{4\pi d_z^2} n_{\rm p} \int_{E_\nu}^{\infty} \sigma_{\rm pp} \frac{dN_{\rm p}}{dE_{\rm p}} F_{\nu_\mu}^{\rm pp}(E_{\rm p}, x) \frac{dE_{\rm p}}{E_{\rm p}}, \quad (9)$$

where the function $F_{\nu_\mu}^{\rm pp}$ is split in two parts (Kelner et al. 2006): one coming from the decay of muons $\mu \rightarrow e\bar{\nu}_{\rm e}\nu_\mu$ ($F_{\nu_\mu^{(2)}}^{\rm pp}$) and the pion decay $\pi \rightarrow \mu\nu_\mu$ ($F_{\nu_\mu^{(1)}}^{\rm pp}$).

4.4.3. Neutrino Expectation

The expected number of reconstructed neutrino events in the IceCube experiment can be computed as (Fraija 2014b, 2014c)

$$N_{ev} = T\, N_A \int_{E_\nu^{th}} \sigma_{\nu N}(E_\nu)\, M_{\rm eff}(E_\nu) \frac{dN_\nu}{dE_\nu} dE_\nu, \quad (10)$$

where $T \simeq 4$ years is the observation time, $N_{\rm A} = 6.022 \times 10^{23}\, {\rm g}^{-1}$ is the Avogadro number, $\sigma_{\nu N}(E_\nu) = 6.78 \times 10^{-35} {\rm cm}^2 (E_\nu/{\rm TeV})^{0.363}$ is the neutrino–nucleon cross section (Gandhi et al. 1998), $M_{\rm eff}(E_\nu)$ is the effective target mass of the IceCube experiment (IceCube Collaboration 2013), and the neutrino spectrum dN_ν/dE_ν is computed from hadronic interactions (Fraija 2015; Fraija & Marinelli 2015). The best function that reproduces the effective target mass is given by (Fraija 2016)

$$M_{\rm eff} = \begin{cases} f_6(E_\nu), & 1\ {\rm TeV} < E_\nu < 950\ {\rm TeV} \\ 5.19 \times 10^{-3}\left(\frac{E_\nu}{\rm TeV}\right) + 3.86 \times 10^2, & \\ 950{\rm TeV} < E_\nu < 10^4{\rm TeV}, & \end{cases}$$

where

$$f_6(E_\nu) = 2.46 \times 10^{-15}\left(\frac{E_\nu}{\rm TeV}\right)^6 - 1.99 \times 10^{-12}\left(\frac{E_\nu}{\rm TeV}\right)^5 - 1.09 \times 10^{-8}\left(\frac{E_\nu}{\rm TeV}\right)^4 + 2.07 \times 10^{-5}\left(\frac{E_\nu}{\rm TeV}\right)^3 - 1.38 \times 10^{-2}\left(\frac{E_\nu}{\rm TeV}\right)^2 + 3.91\left(\frac{E_\nu}{\rm TeV}\right) - 35.3.$$

It is worth noting that the muon neutrino of the effective target mass was used.

5. DISCUSSION

5.1. Hadronic Scenario

The GeV–TeV γ-ray SED of VER J2019+407 is shown in Figure 2. The gigaelectronvolt Fermi LAT fluxes are obtained in this work, and the teraelectronvolt data are taken from the VERITAS observation (Aliu et al. 2013). As can be seen, the Fermi LAT SED connects smoothly with the data at the highest energies. We present the results of fitting the γ-ray SED with a χ^2 minimization as implemented in the ROOT software package (Brun & Rademakers 1997) in Table 1 and the resulting parameters associated with each fitting function. We can see that a broken power law best describes the overall GeV–TeV γ-ray SED and adopt the parent proton distribution given by Equation (6) with $\Gamma_l = \alpha_{\rm p}$ and $\Gamma_h = \beta_{\rm p}$ to calculate the γ-ray emission in a hadronic scenario. The resulting total

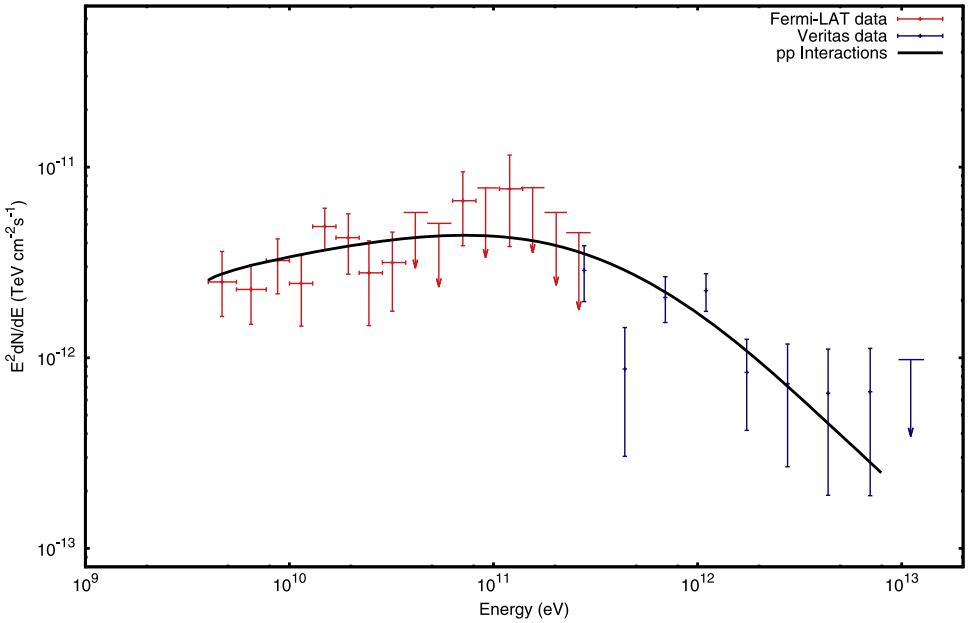

Figure 2. GeV–TeV γ-ray SED of VER J2019+407. The solid line is the broken power-law function that best fits the Fermi LAT fluxes (obtained in this work) and the VERITAS data, as shown in Table 1.

Table 1
Fitting Results for the GeV–TeV Spectrum of VER J2019+407

Spectral shape	Parameters	Values	χ^2/dof
Simple power law			
Spectral index	Γ	2.18 ± 0.03	1.38
Power law with cutoff			
Spectral index	Γ	2.07 ± 0.07	1.20
Cutoff energy	$E_{\gamma,c}$ (TeV)	3.55 ± 2.39	
Broken power law[a]			
Low spectral index	Γ_l	1.78 ± 0.15	
High spectral index	Γ_h	2.46 ± 0.11	1.02
Break energy	$E_{\gamma,br}$ (GeV)	70.7 ± 0.1	

Note.
[a] Γ_l and Γ_h are the spectral indices below and above the break energy $E_{\gamma,br}$.

energy in CR hadrons in this model is $1.95 \times 10^{50}\left(\frac{n_p}{1\ \mathrm{cm}^{-3}}\right)^{-1}$ erg for $p_0 = 1$ TeV and a source distance of 1.5 kpc. The break momentum in the particle distribution is 0.45 TeV.

The CR distribution below the break is harder than predicted for standard test-particle shock acceleration but could be accounted for by nonlinear effects such as shock modification by cosmic rays (Berezhko & Ellison 1999; Malkov 1999). As discussed by Abdo et al. (2009), the break in the proton spectrum could be related to the effects of damping of magnetohydrodynamic turbulence due to ion–neutral collisions in a zone of interaction of the shock with ambient material, assuming that this break is not intrinsic to the acceleration process and that acceleration takes place near the Bohm limit (Baring et al. 1999).

The leptonic emission in this model is calculated with a power-law electron distribution with an index of 2.3, a cutoff particle energy of 20 GeV, and a magnetic field of 9.5 μG. The total lepton energy is 7.7×10^{48} erg, and the ambient density used to calculate the bremsstrahlung emission is the same as that used for the hadronic component, 1 cm^{-3}. The resulting SED and model are shown in Figure 3. We use a bremsstrahlung model similar to the one by Uchiyama et al. (2002) to account for the hard X-ray emission. Although a steeper electron distribution could be used to lower the bremsstrahlung contribution at γ-ray energies, we chose instead to place a cutoff in the electron distribution above a particle energy of 20 GeV.

Considering the resulting neutrino counterpart from pp interactions in this source (Equation (6)), using the values found for the indices (α_p and β_p), the total energy in the hadrons, the break momentum in the particle distribution, and the target mass of the IceCube experiment (Equation (11)), we have computed the number of neutrinos expected in the IceCube detector, and we find that more than 10^3 years of data collection are needed to detect one event at dozens of teraelectronvolts.

5.2. Leptonic Scenario

We find that a simple scenario where a population of HE electrons whose energy distribution is a power law producing gamma rays through IC scattering of CMB photons cannot reproduce the gamma-ray data for reasonable distribution index values. One of the main issues with this scenario is that it cannot account for the hard X-ray fluxes seen by ASCA. This has already been noted by Uchiyama et al. (2002). They ruled out synchrotron (and IC) as the origin of the X-ray emission and conclude that a plausible scenario to account for the observations is nonthermal bremsstrahlung from HE electrons, as would be expected from Coulomb interactions that give rise to a hard X-ray spectrum. We adopt parameters similar to those adopted by these authors for the models, such as a magnetic field of 9 μG, a particle spectral index of 2.3, and a cutoff electron energy of 10 TeV.

The radio flux from the electrons predicted by Uchiyama et al. (2002) is about 10% of the total flux from the SNR, which is in agreement with the observation at 10.6 GHz. However, their SED models overpredict the γ-ray fluxes. We then take

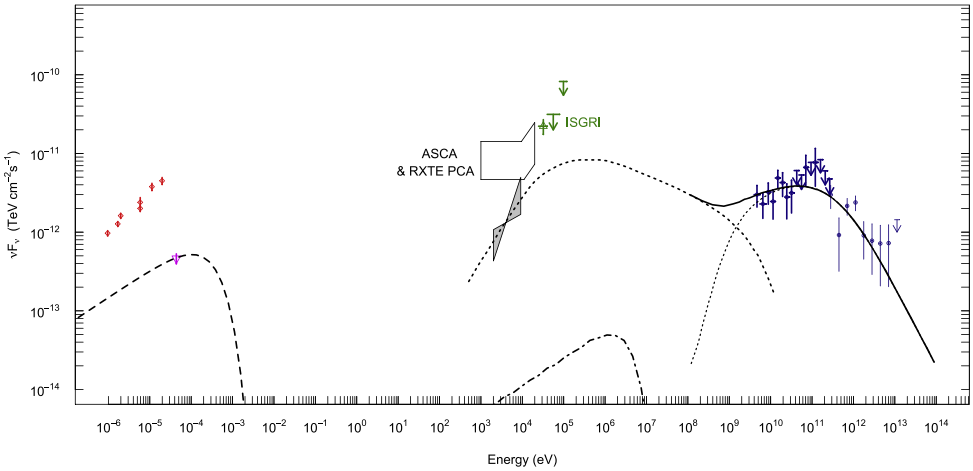

Figure 3. Hadronic model for VER J2019+407. The radio SED points of the integrated emission from the SNR are shown in red, while the magenta triangle shows a 10.6 GHz flux from a $7' \times 9'$ region within VER J2019+407 (Higgs 1977). The ASCA and *RXTE* PCA observation of the remnant and an *INTEGRAL*-ISGRI observation of a clump to the west of VER J2019+407 are shown for reference (Bykov et al. 2004). The shaded region corresponds to the ASCA observation of hard X-ray clumps seen in the region of teraelectronvolt emission as published by Uchiyama et al. (2002). The model components are synchrotron (dashed line), nonthermal bremsstrahlung (dotted line, ambient density $n_{\rm p} = 1\ {\rm cm}^{-3}$), IC-CMB (dash-dotted line), hadronic emission (thin dotted line, ambient density $n_{\rm p} = 1\ {\rm cm}^{-3}$), and the total (solid line).

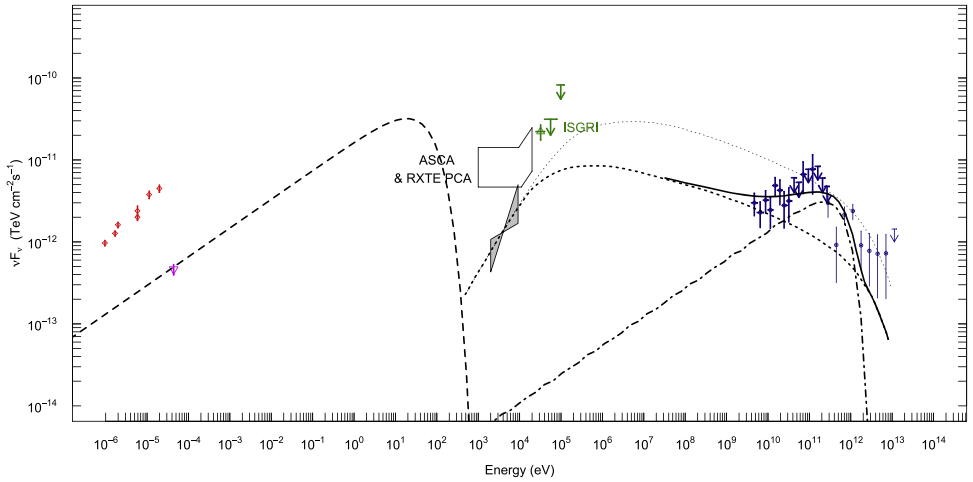

Figure 4. Leptonic model for VER J2019+407. The data shown are the same as in Figure 3. The model components are synchrotron (dashed line), nonthermal bremsstrahlung (dotted line, ambient density $n_{\rm p} = 1\ {\rm cm}^{-3}$), IC-CMB (dash-dotted line), and total gamma-ray emission (solid line). The thin dotted line shows the bremsstrahlung model by Uchiyama et al. (2002), which they calculated for similar parameters except an ambient density of $n_{\rm p} = 10\ {\rm cm}^{-3}$ and which overpredicts the measured fluxes.

their emission model for an electron distribution index of 2.3 and a gas density of $10\ {\rm cm}^{-3}$ and scale it down for a lower density value of $1\ {\rm cm}^{-3}$. We also estimate the kinetic electron energy below which the particle spectrum flattens by equating the source age (7000 years) to the cooling time due to Coulomb interactions, which gives the result $K_{\rm Cou} \sim 0.22$ MeV, and we note that the bremsstrahlung spectrum can be described by a broken power law, with the index above some photon energy in the hard X-ray regime equal to that of the particle spectral index and increasing by one power below this energy (Uchiyama et al. 2002). The resulting model is shown in Figure 4 together with the expected IC-CMB contribution. The total lepton energy is 7.7×10^{48} erg for a magnetic field of 9 μG. This simple leptonic scenario is able to account for the γ-ray fluxes reasonably well, although an improved model, which is beyond our main objective in this work, could consider distinct emitting zones with different spectral and ambient properties.

6. CONCLUSION

With an analysis of Fermi LAT data, we have found a region of enhanced hard gigaelectronvolt emission within the shell of SNR G78.2+2.1 that is in spatial coincidence with the teraelectronvolt source VER J2019+407. The joint GeV–TeV spectrum can be best described with a broken power law. We cannot rule out the leptonic or the hadronic mechanism for the origin of the γ-rays.

A simple leptonic scenario with nonthermal bremsstrahlung and IC emission can account for the gamma-ray SED. Bremsstrahlung emission dominates at low γ-ray energies and is able to explain the hard X-ray emission seen by ASCA in clumps within the extent of VER J2019+407 with an average ambient density of $1\ {\rm cm}^{-3}$ and a magnetic field of 9 μG, for a total particle energy of 7.7×10^{48} erg.

In the hadronic scenario, the required spectral index of the particle population is lower than the standard result from diffusive shock acceleration, but this could be explained by

nonlinear effects (Malkov 1999; Berezhko & Ellison 1999). The origin of the spectral break is also of theoretical interest. The total energy in the particles is within expected values, $\sim 1.95 \times 10^{50} \left(\frac{n_{\rm p}}{1\ {\rm cm}^{-3}}\right)^{-1}$ erg. In this scenario, the leptonic emission can be suppressed with a particle cutoff energy of 20 GeV. A considerable amount of nonthermal bremsstrahlung emission is expected around several hundred megaelectronvolts if the hard X-rays are indeed associated with the HE electrons in the SNR. Detection of synchrotron emission from the northern shell above a frequency of 11 GHz could help quantify the maximum lepton energy and thus the amount of bremsstrahlung γ-ray emission. We point out that it is certainly possible to have a scenario with mixed bremsstrahlung and hadronic emissions, depending, among other parameters, on the true electron power-law index in the northern shell. We computed the neutrino flux resulting from pp interactions and also estimated the number of events expected in the IceCube detector. We found that $\sim 10^3$ years of data collection are needed to observe one event at dozens of teraelectronvolts.

From our analysis, there is an indication that the southern shell of the SNR has a softer gigaelectronvolt spectrum, and indeed this region is not detected at teraelectronvolt energies. Observations yielding the magnetic field values and its geometry or the presence of dense material such as molecular clouds and other ambient properties to the north of G78.2+2.1 could help explain whether the enhanced gamma-ray emission is due to an increase in acceleration efficiency or the result of abundant target material in the case of the hadronic scenario. A detailed analysis of the LAT emission below ~4 GeV is required to better constrain the model parameters and the nature of the radiation. We carried out a preliminary analysis of LAT data above 1 GeV which indicates that the source spectrum becomes softer, as predicted by the models in the previous section. However, we cannot say if this is an artifact from contamination by emission from the bright pulsar within the shell of the SNR.

We thank the anonymous referee for a critical reading of the paper and valuable suggestions that helped improve the quality and clarity of this work. We are also grateful to PAPIIT-UNAM IG100414 and Universidad de Costa Rica for financial support. This research has made use of NASA's Astrophysical Data System and the Canadian Galactic Plane Survey (CGPS), which is a Canadian project with international partners. The Dominion Radio Astrophysical Observatory is operated as a national facility by the National Research Council of Canada. The CGPS is supported by a grant from the Natural Sciences and Engineering Research Council of Canada.

REFERENCES

Abdo, A. A., Ackermann, M., Ajello, M., et al. 2009, ApJL, 706, L1
Abdo, A. A., Ackermann, M., Ajello, M., et al. 2010a, ApJS, 188, 405
Abdo, A. A., Ackermann, M., Ajello, M., et al. 2010b, ApJ, 718, 348
Abdo, A. A., Ackermann, M., Ajello, M., et al. 2010c, ApJL, 710, L92
Abdo, A. A., Ackermann, M., Ajello, M., et al. 2010d, ApJ, 722, 1303
Abdo, A. A., Ackermann, M., Ajello, M., et al. 2010e, Sci, 327, 1103
Abdo, A. A., Ackermann, M., Ajello, M., et al. 2010f, ApJ, 712, 459
Abdo, A. A., Ackermann, M., Ajello, M., et al. 2010g, ApJS, 187, 460
Abdo, A. A., Allen, B., Berley, D., et al. 2007, ApJL, 658, L33
Acero, F., Ackermann, M., Ajello, M., et al. 2015, ApJS, 218, 23
Ackermann, M., Ajello, M., Allafort, A., et al. 2011, Sci, 334, 1103
Aharonian, F. A., Atoyan, A. M., & Kifune, T. 1997, MNRAS, 291, 162
Ajello, M., Allafort, A., Baldini, L., et al. 2012, ApJ, 744, 80
Aliu, E., Archambault, S., Arlen, T., et al. 2013, ApJ, 770, 93
Amato, E., Guetta, D., & Blasi, P. 2003, A&A, 402, 827
Ammosov, A. E., Ksenofontov, L. T., Nikolaev, V. S., & Petukhov, S. I. 1994, AstL, 20, 157
Araya, M. 2013, MNRAS, 434, 2202
Araya, M. 2014, MNRAS, 444, 860
Araya, M. 2015, ApJ, 813, 3
Atwood, W., Albert, A., Baldini, L., et al. 2013, arXiv:1303.3514
Baring, M. G., Ellison, D. C., Reynolds, S. P., Grenier, I. A., & Goret, P. 1999, ApJ, 513, 311
Bartoli, B., Bernardini, P., Bi, X. J., et al. 2014, ApJ, 790, 152
Bell, A. R. 1978, MNRAS, 182, 147
Berezhko, E. G., & Ellison, D. C. 1999, ApJ, 526, 385
Berezhko, E. G., Ksenofontov, L. T., & Völk, H. J. 2002, A&A, 395, 943
Blandford, R., & Eichler, D. 1987, PhR, 154, 1
Blumenthal, G. R., & Gould, R. J. 1970, RvMP, 42, 237
Braun, R., & Strom, R. G. 1986, A&AS, 63, 345
Brazier, K. T. S., Kanbach, G., Carramiñana, A., Guichard, J., & Merck, M. 1996, MNRAS, 281, 1033
Brun, R., & Rademakers, F. 1997, NIMPA, 389, 81
Bykov, A. M., Krassilchtchikov, A. M., Uvarov, Y. A., et al. 2004, A&A, 427, L21
Cheng, K. S., Cheung, T., Lau, M. M., Yu, K. N., & Kwok, P. W. 1990, JPhG, 16, 1115
Downes, D., & Rinehart, R. 1966, ApJ, 144, 937
Ellison, D. C., Patnaude, D. J., Slane, P., & Raymond, J. 2010, ApJ, 712, 287
Fraija, N. 2014a, ApJ, 783, 44
Fraija, N. 2014b, MNRAS, 441, 1209
Fraija, N. 2014c, MNRAS, 437, 2187
Fraija, N. 2015, APh, 71, 1
Fraija, N. 2016, JHEAp, 9, 25
Fraija, N., & Marinelli, A. 2015, APh, 70, 54
Fukui, Y., & Tatematsu, K. 1988, in IAU Coll. 101, Supernova Remnants and the Interstellar Medium, ed. R. S. Roger, & T. L. Landecker (Cambridge: Cambridge Univ. Press), 261
Gandhi, R., Quigg, C., Reno, M. H., & Sarcevic, I. 1998, PhRvD, 58, 093009
Gao, X. Y., Han, J. L., Reich, W., et al. 2011, A&A, 529, A159
Gosachinskij, I. V. 2001, AstL, 27, 233
Gotthelf, E. V., Koralesky, B., Rudnick, L., et al. 2001, ApJL, 552, L39
Higgs, L. A. 1977, AJ, 82, 329
Higgs, L. A., Landecker, T. L., & Roger, R. S. 1977, AJ, 82, 718
Higgs, L. A., Landecker, T. L., & Roger, R. S. 1983, AJ, 88, 97
Hwang, U., Decourchelle, A., Holt, S. S., & Petre, R. 2002, ApJ, 581, 1101
IceCube Collaboration 2013, Sci, 342 arXiv:1311.5238
Kelner, S. R., Aharonian, F. A., & Bugayov, V. V. 2006, PhRvD, 74, 034018
Kothes, R., Fedotov, K., Foster, T. J., & Uyanıker, B. 2006, A&A, 457, 1081
Ladouceur, Y., & Pineault, S. 2008, A&A, 490, 197
Lande, J., Ackermann, M., Allafort, A., et al. 2012, ApJ, 756, 5
Landecker, T. L., Roger, R. S., & Higgs, L. A. 1980, A&AS, 39, 133
Leahy, D. A., Green, K., & Ranasinghe, S. 2013, MNRAS, 436, 968
Lozinskaya, T. A., Pravdikova, V. V., & Finoguenov, A. V. 2000, AstL, 26, 77
Malkov, M. A. 1999, ApJL, 511, L53
Mattox, J. R., Bertsch, D. L., Chiang, J., et al. 1996, ApJ, 461, 396
Mavromatakis, F. 2003, A&A, 408, 237
Pipenbrink, A., & Wendker, H. J. 1988, A&A, 191, 313
Rephaeli, Y. 1979, ApJ, 227, 364
Rho, J., Dyer, K. K., Borkowski, K. J., & Reynolds, S. P. 2002, ApJ, 581, 1116
Stecker, F. W. 1973, ApJ, 185, 499
Tanaka, T., Allafort, A., Ballet, J., et al. 2011, ApJL, 740, L51
Taylor, A. R., Gibson, S. J., Peracaula, M., et al. 2003, AJ, 125, 3145
Thompson, D. J., Bertsch, D. L., Dingus, B. L., et al. 1995, ApJS, 101, 259
Uchiyama, Y., Takahashi, T., Aharonian, F. A., & Mattox, J. R. 2002, ApJ, 571, 866
Wendker, H. J., Higgs, L. A., & Landecker, T. L. 1991, A&A, 241, 551
Yuan, Q., Liu, S., Fan, Z., Bi, X., & Fryer, C. L. 2011, ApJ, 735, 120
Zhang, X., Zheng, Y., Landecker, T. L., & Higgs, L. A. 1997, A&A, 324, 641